Optical Transfer Function Identification from Satellite Images

L. M. Mugnier and G. Le Besnerais

Office National d'Études et de Recherches Aérospatiales (ONERA)
BP 72, F-92322 Châtillon cedex, France

ABSTRACT

The on-orbit identification of the transfer function (TF) of a spaceborne optical telescope is useful for the acceptance test of the instrument, for the on-orbit refocusing and for the restoration of the recorded images. An original method is presented to perform such an identification from a single image. It is based on a physical modeling of the TF *via* the optical aberrations of the instrument, and on the automatic extraction of sub-images containing patterns that can be described with few parameters, e.g. step functions. The estimation of the TF is performed by minimizing a least-square criterion incorporating all extracted sub-images, as a function of the unknowns, which are the aberrations and the step parameters. Aliasing is explicitely incorporated in the image modeling, so that the transfer function can be estimated up to the optical cutoff frequency. The method is validated first on simulated images of step functions, then on a realistic, undersampled and noisy simulated image.

Keywords: wavefront sensing, optical transfer functions, remote sensing, deconvolution, image restoration, inverse problems, telescopes.

1. INTRODUCTION AND PROBLEM STATEMENT

The on-orbit calibration of the transfer function (TF) of a spaceborne telescope may be performed using resolution targets, but this reduces the time available for observations. Methods not needing the acquisition of such special purpose images are thus preferable. Yet, estimating the TF from a single image is a difficult problem, as both the TF and the object are unknown. Additionally, in real-world instruments, the images are not only noisy but also undersampled, so that the TF estimation can be biased by aliasing effects.

The recorded image i is modeled as the noisy sampled convolution of the observed object o (Earth scene) with the instrument's PSF h:

$$i = [h \star o]_{\text{III}} + n, \tag{1}$$

where $[\cdot]_{\text{III}}$ denotes the sampling operator. This model is adequate, at least piecewise in the image, for satellite imaging.

The problem at hand is to estimate the PSF h (or equivalently the TF $\tilde{h} = FT(h)$) from the image i and our prior knowledge on the instrument. Indeed, because we are concerned with on-orbit calibration, the instrument is partially known either from its detailed opto-electronic design or from ground calibrations prior to launch. Hence we assume that parameters such as the linear central obscuration, the detector transfer function (DTF), and the ratio f_c/f_n of the optical cutoff frequency to the detector's Nyquist frequency, are known.

One is interested in a precise characterization of the two-dimensional (2-D) TF, especially in the high frequency domain. Such a characterization is useful for the acceptance test of the instrument, for the on-orbit refocusing and for the restoration of the recorded images. As most real-world instruments are undersampled, estimation of the high frequencies of the instrument response should explicitly model the aliasing.

This problem is akin to blind deconvolution, as both the object and the instrument are unknown. However, BD aims at restoring the object while the method proposed herein aims at a precise characterization of the OTF of the instrument. Therefore, BD usually considers the TF characteristics as nuisance parameters and uses simple spatial-domain models of the aliased instrument's response (with exceptions, notably the approach of Schulz and Cain[1]).

Another difference between the method proposed here and BD resides in the type of processing performed on the image. In BD, the whole image is processed in order to yield an estimate of the TF; this processing either consists in a joint estimation of the TF and the object, or in a marginal estimation of the sole TF, for instance in a maximum likelihood framework.[2,3] In both cases the object model (by, e.g., a Markov random field) has many unknown object parameters (usually pixel values). The

Other author information: Email: `mugnier@onera.fr` ; URL: http://www.onera.fr/dota

main problem of BD is to avoid confusions between the object and the instrument : for instance a smooth edge in the image can be the result of a smooth object edge seen though a high resolution instrument or of a crisp object edge smoothed by a low resolution instrument.

Consequently, unless some additional prior knowledge is available on the object (e.g., it is a star field) and/or on the TF (e.g., through an optical parametric model), the TF estimate is often imprecise in the BD context.

Our approach is closer to conventional calibration on resolution targets. Indeed, we focus the estimation on parts of the image which can be viewed as opportunistic resolution targets and which can be described by simple parametric models, e.g., step functions, similarly to Refs. 4 and 5. We propose to use a physical modeling of the TF: it is parameterized by the optical aberrations of the instrument expanded on (a limited number of) Zernike polynomials, as first proposed for the BD of turbulence-degraded images.[6] Moreover, we explicitly take aliasing effects into account in our image model.

Section 2 is devoted to the principle of the TF estimation method from a set of selected sub-images. Section 3 validates the estimation method by means of simulations. Section 4 discusses the automatic selection of suitable sub-images from the whole image. Section 5 illustrates the performance of the complete extraction plus estimation process on a realistic simulated image.

2. TRANSFER FUNCTION ESTIMATION

2.1. Instrument model

The instrument is assumed to be partially known. Its TF $\tilde{h}$ is modeled as the product of the known DTF $\tilde{h}_{\text{det}}$ with the optical transfer function (OTF) $\tilde{h}_{\text{opt}}$:

$$\tilde{h} = \tilde{h}_{\text{opt}} \times \tilde{h}_{\text{det}}. \tag{2}$$

The OTF is modeled through the aberrations (or phase) φ in the instrument's pupil[7] expanded on the first Zernike polynomials Z_l:

$$\varphi(x,y) = \sum_{l=4}^{11} a_l Z_l(x,y). \tag{3}$$

Indeed in a space telescope there are essentially low order aberrations, which we here limit to Zernike polynomials Z_4 (defocus) to Z_{11} (spherical aberration). The unknown of interest is the OTF but these aberrations allow us to parameterize the latter with few, physically meaningful coefficients. Assuming that the spectral bandwidth is small compared to the central wavelength, the OTF is related to the aberrations in the pupil through[7]:

$$\tilde{h}_{\text{opt}} = \text{FT}\left(\left| \text{FT}^{-1}(P(x,y)e^{j\varphi(x,y)}) \right|^2 \right), \tag{4}$$

where P is the pupil (or aperture) function, and FT denotes the Fourier transform. Lastly, the ratio f_c/f_n of the OTF's cutoff to the detector's Nyquist frequency is assumed to be known, and will be taken as 1 or 2 in the following.

2.2. Considered sub-images: linear features

The TF estimation is performed on sub-images which should have a high frequency (HF) content, accept a simple parametric model, and be sufficiently numerous in an image to lead to a reasonable statistical contrast. Linear features such as linear edges meet all these conditions and are often used in instrument calibration.

Let us recall some basic properties of linear features, which are known as the Radon or "Fourier slice" theorem and will be used in the following to reduce the computational burden of the criterion to 1-D computations. A linear feature with orientation θ and profile p is a 2-D object whose radiometry takes the form $o(x,y) = p(-x\sin\theta + y\cos\theta)$, *i.e.*, is invariant along the direction θ. It is trivial to show that the FT of such a feature lives on a radial line of orientation $\theta+\pi/2$ of the Fourier plane, with a complex amplitude which is the 1-D Fourier transform of the profile p. Thus the image of a linear feature through (1) is a linear feature too, which results from the spreading of an image profile along the direction θ. Additionally, this image profile is in turn the 1-D convolution of the object profile p with a unique 1-D response l_θ called the linear spread function (LSF). Lastly, the LSF is the 1-D inverse Fourier transform of the cut of the 2-D transfer function along the radial line of orientation $\theta+\pi/2$.

Here we focus on linear features whose profile is a step function. These features are described by four parameters, as shown in Fig. 1. Other linear features, such as double step functions, are used in Bones *et al.*[5] and could be used here as an extension of the following developments.

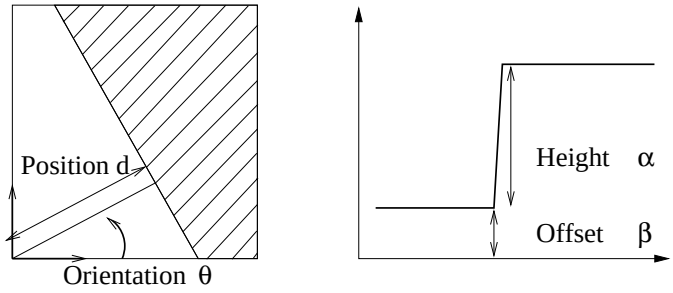

Figure 1. Parameters of a step function: position and orientation (left), height and offset (right).

2.3. Principle of the transfer function estimation

We start with a set of K sub-images $i_1,\ldots,i_k,\ldots,i_K$, whose support S_K may be very different. These sub-images each correspond to an object which is assumed to be a step (or Heavyside) function. This object, denoted by o_k, is fully characterized by its orientation θ_k, its distance to the origin d_k, its height α_k and its lower value (or offset) β_k, as illustrated on Fig. 1.

Because the estimation of the OTF boils down to that of the first aberrations, we shall denote the PSF by $h(\{a_l\}_{l=4}^{11})$. The estimation is performed by minimizing a least square criterion, which is non-linear in the aberrations:

$$J(\{a_l\},\{\theta_k,d_k,\alpha_k,\beta_k\}) = \sum_{k=1}^{K} \sum_{(p,q)\in S_k} |i_k(p,q) - [h(\{a_l\}_{l=4}^{11}) \star o_k(\theta_k,d_k,\alpha_k,\beta_k)](p,q)|^2. \quad (5)$$

This criterion measures the discrepancy between the sub-image models $[h\star o_k]_{\mathrm{III}}$ and the sub-images i_k extracted from the recorded image i. In the case of a stationary white Gaussian noise, which is a reasonable approximation for satellite imaging, minimizing this criterion is equivalent to searching for a maximum likelihood solution.

2.4. Minimization of the criterion

The criterion is minimized jointly in all parameters, which are the aberrations and the object parameters, globally for all sub-images.

An essential step of the minimization of the criterion is its computation, which is essentially that of a sub-image model $[h\star o_k]_{\mathrm{III}}$ for the current parameters. The computation of h is easily performed by using eqs. (2) and (4) and by replacing the FT by an FFT in the latter.

We use the properties of linear features recalled in sub-section 2.2 to compute a sub-image model for a linear edge of orientation θ through the following steps:

1. cut of the transfer function in the direction $\theta+\pi/2$ (60^o on Fig. 2 (a)),
2. zero-padding of the cut (see 2 (b)),
3. inverse FFT leading to an interpolated LSF l_θ (see 2 (c)),
4. numerical integration of the LSF to obtain the step image profile (see 2 (d)),
5. spreading along direction θ of the step image profile oriented along direction $\theta+\pi/2$ (see 2 (e)).

The minimization is accelerated both by analytic considerations and by reasonable approximations. Firstly, the criterion is quadratic in any (α_k,β_k), so that it can be minimized analytically in these variables, as a function of the other unknowns. Secondly, we have checked that the angles θ_k can be estimated precisely without knowing the aberrations, *i.e.*, with a perfect PSF. To do this, we minimize criterion J of Eq. (5) as a function of all (θ_k,d_k) for null aberrations. One notices that the minimization can be performed separately on each variable pair (θ_k,d_k) because each only appears in the k-th term of J.

Thanks to these considerations, the criterion to be minimized then only contains the variables of interest a_l that are related to the OTF, and the distances d_k. Indeed, these must be re-estimated because they code for the step positions, which depend on the shape of the PSF. The minimization is achieved by means of the Powell method, which does not need the analytic expression of the criterion's gradient.

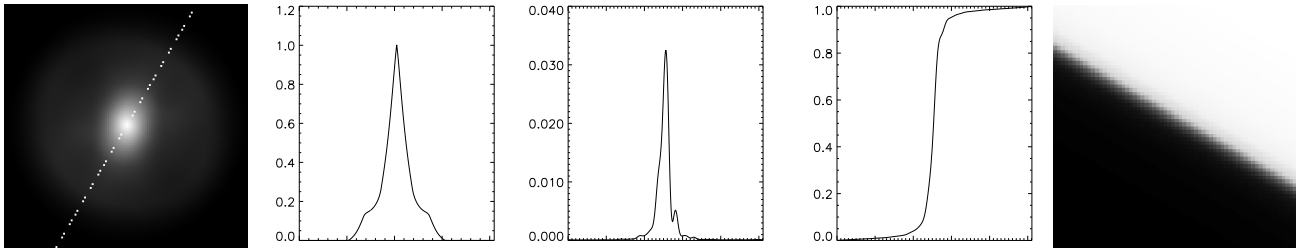

(a) (b) (c) (d) (e)

Figure 2. Computation steps for the sub-image model of a linear edge: cut of the transfer function (a), zero-padding (b), inverse FFT leading to an interpolated LSF (c), numerical integration to obtain the step image profile (d) and 2-D spreading of this profile (e).

3. VALIDATION OF THE ESTIMATION METHOD ON SYNTHETIC IMAGES

A first validation of the method was to estimate the OTF on sub-images that were computed exactly as the sub-image models used for the estimation, *i.e.*, by making use of the Radon theorem mentioned above; the results are very good, but probably not representative of the estimation quality attainable on more realistic images.

In the following, the sub-images are 32×32 and computed by the discrete convolution of an oversampled object with an oversampled PSF, which approximates a continuous convolution and is then sampled appropriately. Thus, a simulated sub-image is not computed in the same way as the corresponding sub-image model during the estimation. This aims at validating the robustness of the estimation with respect to small modeling errors and at preparing the validation on more realistic images such as the one presented in Section 5. We present results obtained with two sets of sub-images; the first one is obtained with the Shannon sampling rate ($f_c/f_n = 1$) while the second one is obtained with a more realistic undersampling of a factor $f_c/f_n = 2$.

The OTF is defined through the 8 first Zernike polynomials; the aberration coefficients are given in Table 1 and make up a total phase variation of $2\pi/8$rd RMS. The linear central obscuration is 26%. The DTF is that of a CCD detector and takes into account the temporal integration along the satellite track. The global transfer function and its two (optical and detector) components are represented on Fig. 3.

Coefficient	a_4	a_5	a_6	a_7	a_8	a_9	a_{10}	a_{11}
Name	defocus	astigm. x	astigm. y	coma x	coma y	triang. coma x	triang. coma y	spherical
Radial order	2	2	2	3	3	3	3	4
Value (rd)	$2\pi/(8\sqrt{5})$	$-2\pi/(8\sqrt{5})$	0	0	$2\pi/(8\sqrt{5})$	0	$2\pi/(8\sqrt{5})$	$-2\pi/(8\sqrt{5})$

Table 1. Aberration mixture used to compute the OTF (note: $2\pi/(8\sqrt{5}) \approx 0,35$rd). The total optical path difference is thus $\lambda/8$.

We first present simulation results with noiseless images. For $f_c/f_n = 1$, even with only two sub-images oriented at 0 and 90°, the estimated transfer function is very good in these directions, as illustrated in Fig. 4. It is very poor in other directions, with a maximum error of 0.13; this illustrates the fact that each sub-image of a step provides information in one direction, perpendicular to the step. When the number of sub-images increases while the steps' orientations diversify, the estimation quickly improves.

For $f_c/f_n = 2$, two sub-images oriented at 0 and 90° do not suffice to obtain a good transfer function estimate in these directions, as illustrated in Fig. 5; the maximum error on the 2-D transfer function is 0.16; in particular, the latter is poorly extrapolated above f_n. This is expected, as the orientations of the sub-images do not allow distinguishing between aliased high spatial frequencies and low spatial frequencies. As soon as the steps' orientations diversify, the estimation quickly improves; in particular, Fig. 6 shows x and y cuts of the transfer function estimate obtained for four sub-images of edges oriented every 45°.

Tables 2 and 3 summarize the transfer function estimation results for two, four and eight noiseless sub-images, with regularly spaced orientations, for $f_c/f_n = 1$ and $f_c/f_n = 2$ respectively. In particular for eight sub-images the maximum estimation error

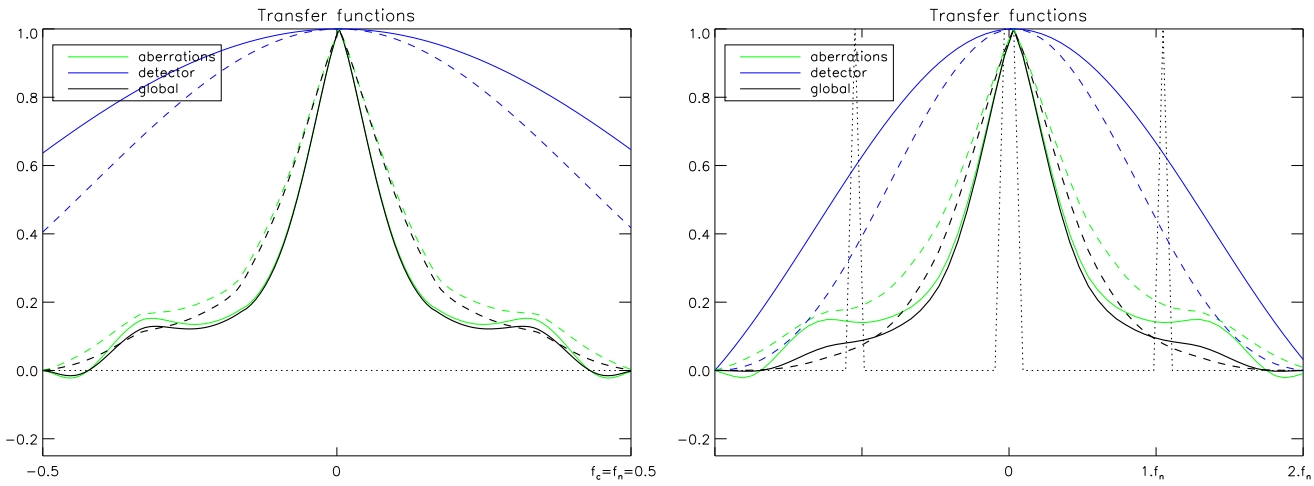

(a) (b)

Figure 3. Transfer functions used for the simulations, obtained as product of the optical TF by the detector TF, for $f_c/f_n = 1$ (a) and $f_c/f_n = 2$ (b). Profiles along x in solid line, along y in dashed line.

over the whole spatial frequency domain is $1.5\,10^{-2}$ and $0.73\,10^{-2}$ for $f_c/f_n = 1$ and $f_c/f_n = 2$ respectively. The fact that the error in the undersampled case is about twice smaller than in the Shannon-sampled case can be attributed to the fact that the transfer function itself, at medium to high frequencies, is about twice smaller in the undersampled case, due to the DTF.

We now consider eight sub-images with the same orientations as above, and assess the robustness of the method with respect to noise. For this purpose, the sub-images are degraded by an additive stationary white Gaussian noise of standard deviation σ_n, and the transfer function is estimated from these eight sub-images. The considered values of σ_n are 1%, $\sqrt{10} \approx 3\%$ and 10% of the image maximum value. The first value is typical of an Earth observing telescope, the second one is a quite noisy case and the third is an extreme case.

For $f_c/f_n = 1$, up to a value of $\sigma_n = 3\%$, the estimation quality remains almost constant and the maximum error remains below 2% (see Table 4); for 10% noise, the error becomes very important and more sub-images would be needed to reach a reasonable maximum error value.

For $f_c/f_n = 2$, the estimation quality is about the same for $\sigma_n = 0\%$ and $\sigma_n = 1\%$, and is below 1%. The error starts off sooner than for $f_c/f_n = 1$, *i.e.*, from $\sigma_n = 3\%$ on, because an aliased PSF is coded with less pixels than a correctly sampled one so that, again, more sub-images would be needed to reach a reasonable maximum error value.

# of sub-images	2	4	8
Maximum error	$13\,10^{-2}$	$1.8\,10^{-2}$	$1.5\,10^{-2}$
MSE	$3.5\,10^{-2}$	$0.47\,10^{-2}$	$0.40\,10^{-2}$

Table 2. Maximum error and mean-square error (MSE) on the transfer function estimation for two, four and eight noiseless sub-images with correct sampling.

# of sub-images	2	4	8
Maximum error	$16\,10^{-2}$	$0.87\,10^{-2}$	$0.73\,10^{-2}$
MSE	$3.2\,10^{-2}$	$0.19\,10^{-2}$	$0.17\,10^{-2}$

Table 3. Maximum error and mean-square error (MSE) on the transfer function estimation for two, four and eight noiseless sub-images undersampled by a factor 2.

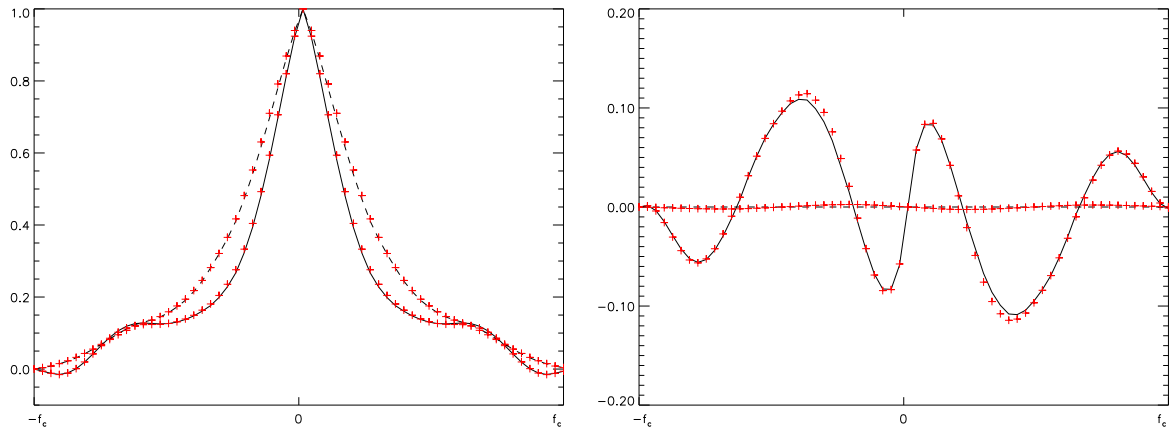

Figure 4. Profiles of the estimated (+++) and true (— along x, – – – along y) transfer functions from 2 noiseless 32×32 sub-images with correct sampling. Left: real part; right: imaginary part.

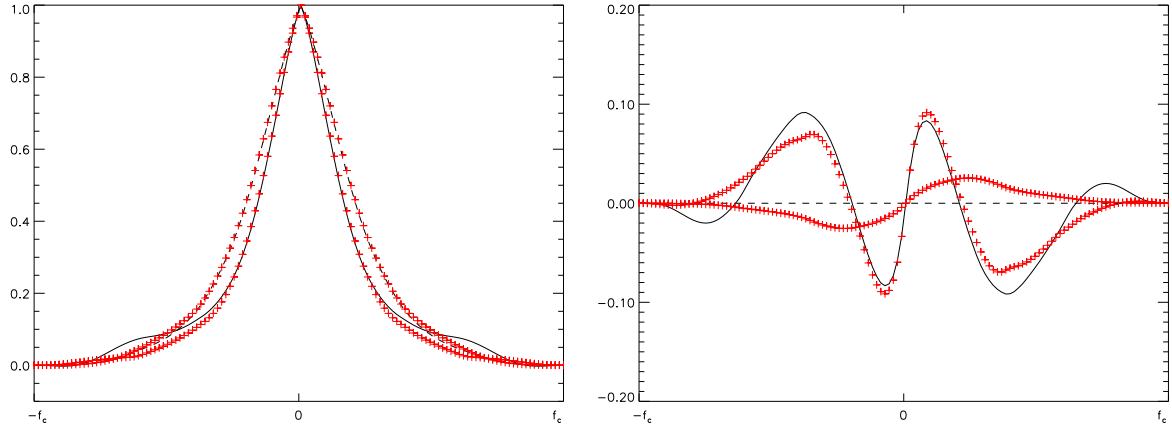

Figure 5. Profiles of the estimated (+++) and true (— along x, – – – along y) transfer functions from 2 noiseless 32×32 sub-images undersampled by a factor 2. Left: real part; right: imaginary part.

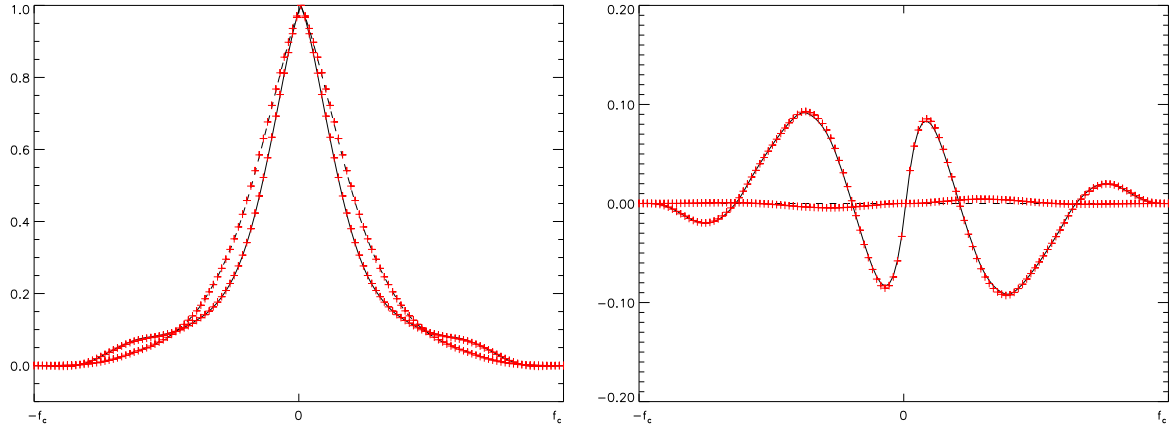

Figure 6. Profiles of the estimated (+++) and true (— along x, – – – along y) transfer functions from 4 noiseless 32×32 sub-images undersampled by a factor 2. Left: real part; right: imaginary part.

σ_n	0%	1%	3.2%	10%
Max. error	$1.5\,10^{-2}$	$1.4\,10^{-2}$	$1.6\,10^{-2}$	$7.6\,10^{-2}$
MSE	$0.40\,10^{-2}$	$0.36\,10^{-2}$	$0.53\,10^{-2}$	$2.1\,10^{-2}$

Table 4. Maximum error and mean-square error (MSE) on the transfer function estimation for eight sub-images with correct sampling, for several noise levels. The noise is stationary white Gaussian, with a standard deviation of 0%, 1%, $\sqrt{10}$% and 10% of the image maximum value respectively.

σ_n	0%	1%	3.2%	10%
Max. error	$0.73\,10^{-2}$	$0.79\,10^{-2}$	$2.2\,10^{-2}$	$4.2\,10^{-2}$
MSE	$0.17\,10^{-2}$	$0.19\,10^{-2}$	$0.48\,10^{-2}$	$0.85\,10^{-2}$

Table 5. Maximum error and mean-square error (MSE) on the transfer function estimation for eight sub-images undersampled by a factor 2, for several noise levels. The noise is stationary white Gaussian, with a standard deviation of 0%, 1%, $\sqrt{10}$% and 10% of the image maximum value respectively.

4. AUTOMATIC EXTRACTION OF THE SUB-IMAGES

The extraction is achieved in two steps. The first step is a fast processing of the whole image, designed to detect the relevant features and to minimize the rate of missed features; the second step further checks the sub-images for consistency with the linear model and aims at minimizing the rate of false alarms.

4.1. Detection step

We use a standard edge detector, *i.e.*, Deriche's implementation of the Canny detector[8] followed by a polygonalization step, in order to extract linear edges in the image. We then select sub-images around edges whose extensions both along the step and orthogonally to it are greater than the assumed PSF diameter d.

Then we use a region growing segmentation starting on both sides of the selected edges to extract the two regions adjacent to the edge and to compute their mean values m_1, m_2 and standard deviations s_1, s_2. Then we select the high-contrast edges bordering uniform regions according to the following criterion:

$$|m_1 - m_2| > 2 * \max(s_1, s_2).$$

4.2. Selection step

The second step further checks the sub-images for consistency with the model of a convolved and noisy step function. This step is akin to sub-pixel localization of edges, as already noted in Ref. 5.

Each sub-image is rotated by bi-cubic interpolation so that the edge is aligned with the vertical axis, using the orientation given by the polygonalization step. Then two tests are conducted on the resulting (horizontal) profiles. Firstly, the variations in each profile near both ends should be consistent with the image SNR. The sub-image is rejected if these variations are above $2\sigma_n$.

Secondly, the central part of the profiles should be essentially sampled and shifted versions of a unique perfect profile, except for the noise. The shifts results from the fact that the orientation of the feature is only approximatively known at this stage: an orientation error results, to the first order, in a linearly growing shift along the edge. We identify sub-pixel shifts for each profile by a least-square fit. This fit is performed by expanding iteratively the interpolation formulae to the first order, similarly to standard motion estimation techniques. As a result, the profiles are precisely aligned with the vertical axis. A linear regression step is then conducted on the vector of shifts. Such a regression accounts for the already mentioned orientation error. The rejection test is conducted on the residual shifts: the sub-image is rejected if the residual shift standard deviation is above a given threshold. Illustrations of this rejection process are given in Fig. 7.

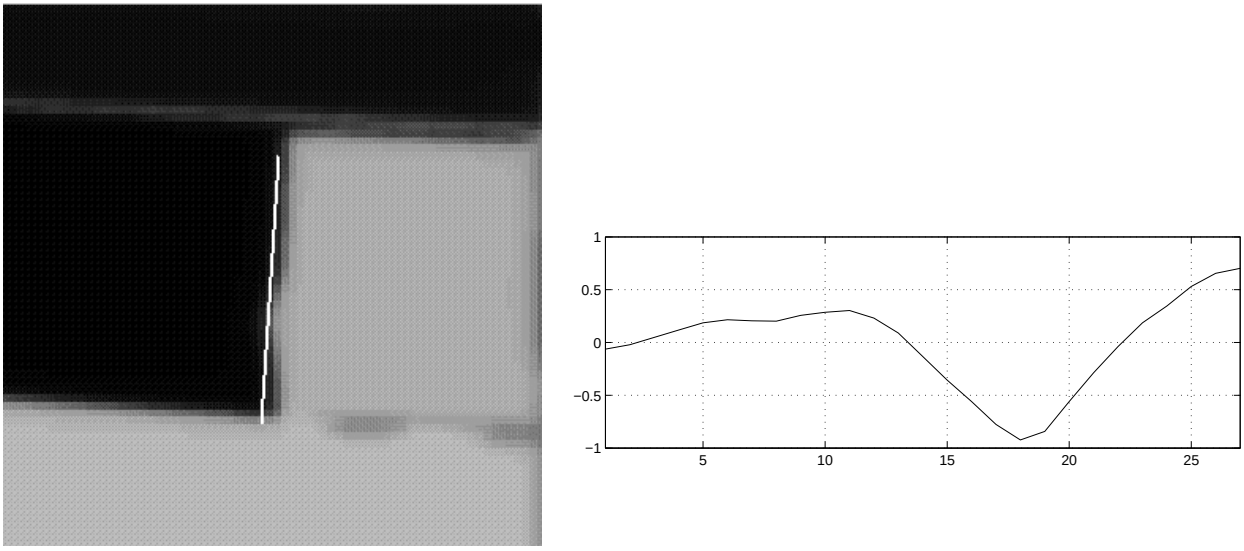

(a) (b)

Figure 7. (a) sub-image with a "bump" and the linear edge detected in the first step: note the position and orientation errors of the detected edge; (b) mean residual shift of the profiles (as a function of the coordinate along the edge): the large oscillation around coordinate 18 is a signature of the bump and leads to a rejection.

4.3. Discussion

Such a two step detection/recognition scheme is classical in pattern recognition and can also be found in Ref. 5. In this reference, the first step is based on the Hough transform[9] to detect linear features which can be either single or double steps. Here, the proposed detection step is tailored for single step detection. The second step of Ref. 5 relies on polynomial fit and is adapted to the large ratio f_c/f_n of Spot images, but could fail for moderate undersampling.

The two main parameters for sub-image extraction are the PSF diameter in pixel, which is inversely proportional to the ratio f_c/f_n, and the signal-to-noise ratio (or more generally the available statistical characteristics of the noise). A difficult threshold to adjust is the threshold for the rejection based on the profiles' residual shifts: it should depend on f_c/f_n, on the SNR and on the length of the segment. This relationship is currently empirically defined. The extraction process has been successfully tested on synthetic images for different noise variances and for two values of f_c/f_n (1 and 2).

5. VALIDATION OF THE GLOBAL METHOD ON A REALISTIC IMAGE

We have used an aerial 1696×1696 metric image of the Grenoble region (©IGN) to generate the object. We could not use the original image itself as an object; indeed, this image was already somewhat smooth because of its acquisition process. So the object was taken as a segmented version of this original image, with gray levels given by the mean level of each region, and piecewise-linear edges.

A 424×424 4m resolution image of this object is obtained by discrete convolution (see the discussion in Sect. 3) and undersampling ($f_c/f_n = 2$). The PSF is the aliased PSF corresponding to Fig. 3 (b), and the standard deviation of the added noise is 1%, or 2.55 gray levels.

Figure 8 shows the image and the detected edges, before the selection step, and Figure 9 shows the 11 sub-images resulting from the extraction (detection and selection). The result of the transfer function estimation is presented in Fig. 10. The maximum error is $3.0\,10^{-2}$, and is only reached for frequencies for which no sub-image provides information.

These results show that a precise estimation of the transfer function is possible even with a small number of sub-images, provided the orientations of these sub-images span 180^o relatively evenly. Additionally, our experience suggests that a severe selection of the detected sub-images is essential, as even a small number of sub-images deviating from the model can bias the estimation. Indeed, we have observed that such deviations systematically lower the HF content of the estimated transfer function. Our interpretation is that if a sub-image deviates from the model (see for instance Fig. 7), the corresponding mean

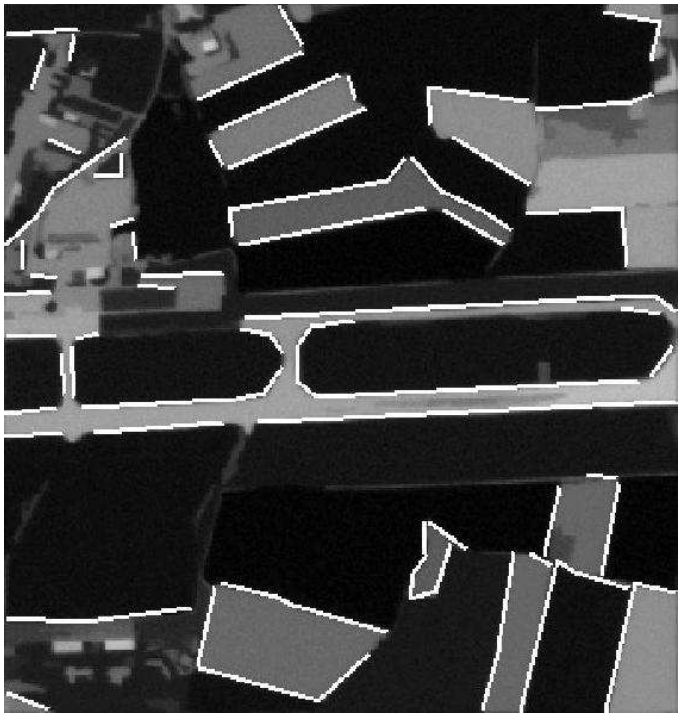

Figure 8. Test image and edges detected by the method described in Sect. 4.1, some of which are rejected by the subsequent selection step (see Fig. 9 for the final result of the extraction).

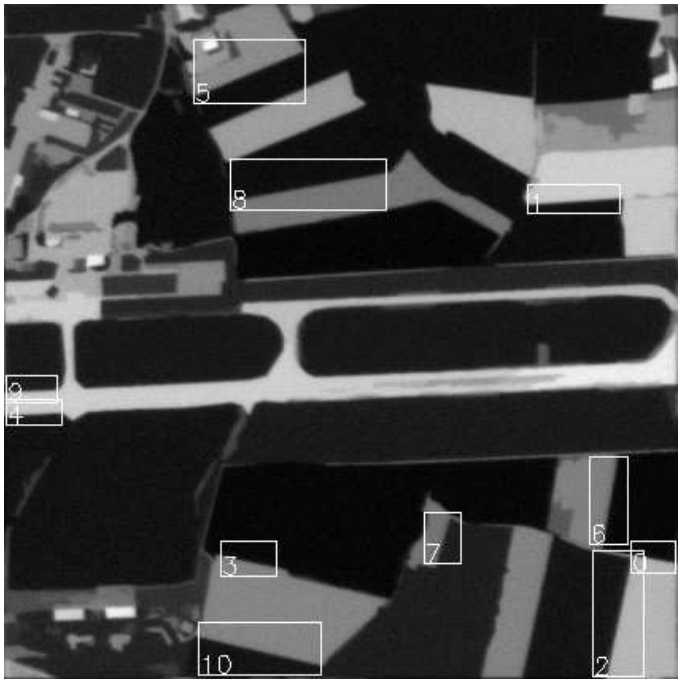

Figure 9. Test image and extracted sub-images.

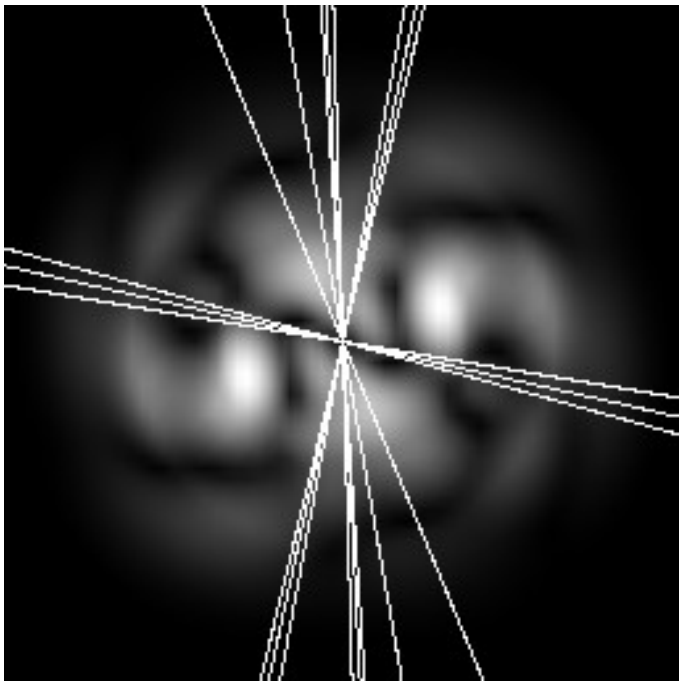

Figure 10. Modulus of the difference between the true transfer function and its estimate. The maximum value is $3.0\,10^{-2}$. The lines indicate the directions orthogonal to the edges of the selected sub-images.

image profile will be smoother than for a true linear edge; the best fit to this profile will then be obtained for a smoother PSF than the true one.

6. CONCLUSION

A novel method has been presented for the identification of the transfer function of an optical telescope from a single image. This method can be used both for the performance assessment of the instrument after launch, for the on-orbit refocusing and for the restoration of the images recorded by the instrument. This method is based on: (1) a physical modeling of the transfer function *via* the optical aberrations of the instrument; (2) the detection and selection of sub-images containing features such as natural step functions that can be parameterized easily; (3) the global transfer function estimation from the set of all sub-images by a least-square criterion minimization which is non-linear in the unknown aberrations.

The estimation part of this method has first been validated of simulated sub-images of step functions, for several sets of sub-images, two undersampling ratios and various noise levels. Then, the complete sub-image extraction and transfer function estimation procedure has been validated on a realistic, undersampled and noisy image. Future work include:

- taking into account other features, such as lines and double edges, to increase the number of useful sub-images;
- investigating the influence of the spectral bandwidth of the instrument;
- enhancing the automatic tuning of some of the threshold parameters for the detection and selection of the sub-images. These parameters are currently related simply to f_c/f_n and to the noise level; this relation deserves further investigation;
- further validating the method on experimental images.

ACKNOWLEDGMENTS

The authors thank Frédéric Champagnat and Vincent Michau for fruitful discussions.

REFERENCES

1. T. J. Schulz and S. C. Cain, "Simultaneous phase retrieval and deblurring for the Hubble space telescope," in *The Restoration of HST Images ans Spectra II*, R. J. Hanisch and R. L. White, eds., pp. 206–211, Space Telescope Science Institute, 1994.
2. A. K. Katsaggelos, ed., *Digital Image Restoration*, Springer Series in Information Sciences, Springer-Verlag, Berlin, 1991.
3. A. Jalobeanu, L. Blanc-Féraud, and J. Zerubia, "étude de la restitution des paramètres instrumentaux en imagerie satellitaire," Tech. Rep. 3957, INRIA, June 2000.
4. B. Forster and P. Best, "Estimation of SPOT P-mode point spread function and derivation of a deconvolution filter," *Journal of Photogrammetry and Remote Sensing* **49**, pp. 32–42, 1994.
5. P. J. Bones, T. Bretschneider, C. J. Forne, R. P. Millane, and S. J. McNeill, "Tomographic blur identification using image edges," in *Image Reconstruction from Incomplete Data*, vol. 4123, 2000.
6. T. J. Schulz, "Multiframe blind deconvolution of astronomical images," *J. Opt. Soc. Am. A* **10**(5), pp. 1064–1073, 1993.
7. M. Born and E. Wolf, *Principles of Optics*, Pergamon Press, Sixth (corrected) ed., 1993.
8. R. Deriche, "Using Canny's criteria to derive a recursively implemented edge detector," *IJCV* **1**, pp. 167–187, May 1987.
9. R. Duda and P. Hart, "Use of the Hough transform to detect lines and curves in pictures," *Commun. ACM* **15**, 1972.